Time-dependent complete-active-space self-consistent-field method for atoms: Application to high-order harmonic generation

Takeshi Sato, Kenichi L. Ishikawa, Iva Březinová, Fabian Lackner, Stefan Nagele, and Joachim Burgdörfer

Phys. Rev. A **94**, 023405 — Published 9 August 2016

DOI: 10.1103/PhysRevA.94.023405

Time-dependent complete-active-space self-consistent-field method for atoms: Application to high-harmonic generation

Takeshi Sato* and Kenichi L. Ishikawa†
Photon Science Center, School of Engineering, The University of Tokyo, 7-3-1 Hongo, Bunkyo-ku, Tokyo 113-8656, Japan and Department of Nuclear Engineering and Management, School of Engineering, The University of Tokyo, 7-3-1 Hongo, Bunkyo-ku, Tokyo 113-8656, Japan

Iva Březinová, Fabian Lackner, Stefan Nagele, and Joachim Burgdörfer
Institute for Theoretical Physics, Vienna University of Technology, Wiedner Hauptstraße 8-10/136, 1040 Vienna, Austria, EU

We present the numerical implementation of the time-dependent complete-active-space self-consistent-field (TD-CASSCF) method [Phys. Rev. A, **88**, 023402 (2013)] for atoms driven by a strong linearly polarized laser pulse. The present implementation treats the problem in its full dimensionality and introduces a gauge-invariant frozen-core approximation, an efficient evaluation of the Coulomb mean field scaling linearly with the number of basis functions, and a split-operator method specifically designed for stable propagation of stiff spatial derivative operators. We apply this method to high-harmonic generation in helium, beryllium, and neon and explore the role of electron correlations.

PACS numbers: 32.80.Rm, 31.15.A-, 42.65.Ky

I. INTRODUCTION

The rapid progress in experimental techniques for ultrashort optical light sources with high-intensity has opened new research areas including ultrafast molecular probing [1–3], attosecond science [4–6], and XUV nonlinear optics [7, 8], with the ultimate goal to directly measure, and even control electron motion in atoms, molecules, and solids. The time-dependent Schrödinger equation (TDSE) provides the rigorous theoretical framework for investigating electron dynamics [9–24]. However, direct real-space solutions of the TDSE for systems with more than two electrons remain a major challenge.

To investigate multi-electron dynamics in intense laser fields, the multiconfiguration time-dependent Hartree-Fock (MCTDHF) method has been developed [25–29] in which the time-dependent total wave function is given in the configuration interaction (CI) expansion,

$$\Psi(t) = \sum_I \Phi_I(t) C_I(t), \tag{1}$$

where $\Phi_I(t)$ is a Slater determinant built from a given number, n, of orbital functions $\{\psi_p(t)\}$ called occupied orbitals. Both the CI coefficients $\{C_I\}$ and the orbitals are simultaneously varied in time which allows to use a considerably smaller number of orbitals than in a standard CI approach. The conventional MCTDHF method is based on the full-CI expansion; the summation I in Eq. (1) is taken over all possible realizations of distributing N electrons among the $2n$ spin orbitals $\{\psi_p\} \otimes \{\uparrow, \downarrow\}$, where $\uparrow$ ($\downarrow$) is the up- (down-)spin eigenfunction. In this article we refer to the term time-dependent multiconfigurational self-consistent field (TD-MCSCF) method in a broader context that involves the multiconfiguration wave function of the form Eq. (1) without the restriction to the full-CI expansion.

Following the first implementations of the MCTDHF method for one-dimensional (1D) model Hamiltonians [25, 26, 28] and with a Gaussian basis set [27], three-dimensional (3D) real-space implementations and their applications have been reported by several authors [30–34]. The 3D implementations have been most successfully applied to cases with short wavelength (high photon energy) pulses. For example, Hochstuhl and Bonitz have presented an application to atoms in spherical polar coordinates and simulated two-photon ionization of helium [32]. Haxton and McCurdy have used spherical polar coordinates and prolate spheroidal coordinates for atoms and diatomic molecules, respectively, and simulated single-photon ionization of a Be atom and a HF molecule [33]. They have also simulated X-ray core excitation and core ionization and subsequent relaxation processes in NO molecules [34]. In contrast to perturbative processes, application of the MCTDHF method to strong-field processes at longer wavelength (visible to infrared) and high intensities (peak intensities up to 10^{15} W/cm^2) such as tunneling ionization and high-harmonic generation (HHG) are largely missing. A few exceptions include the work of Jordan *et al.* [30] who analyzed molecular size effects on strong-field ionization of model two electron systems, and the work of Kato and Kono [31], where single and double ionization of a hydrogen molecule induced by a near-infrared (NIR) laser pulse were investigated. The quantitative first-principles study of multi-electron dynamics in the long-wavelength high-intensity regime still remains a challenge.

One of the difficulties lies in the large CI dimension defined as the expansion length in Eq. (1), required to accurately describe many-electron wave functions. Within the full-CI based MCTDHF method the CI dimension, and therefore, the computational cost increases factorially with the

* Electronic mail:sato@atto.t.u-tokyo.ac.jp
† Electronic mail:ishiken@atto.t.u-tokyo.ac.jp

number of electrons N. To overcome this limitation we have recently proposed the time-dependent complete-active-space self-consistent-field (TD-CASSCF) method [35]. Similar to the stationary CASSCF method of quantum chemistry it makes use of the decomposition into *core* and *active* orbital subspaces. Accordingly, core electrons within the closed-shell wave function are treated closely following the time-dependent Hartree-Fock (TDHF) method [36], while the active electrons are fully correlated among active orbitals as in the MCTDHF method. Whereas, in general, all the orbitals are varied in time, it is possible to further split the core space into time-independent frozen-core (FC) and time-dependent dynamical-core (DC) orbitals (see Fig. 1). With the decomposition into core and active orbitals, the TD-CASSCF method significantly reduces the CI dimension without sacrificing the accuracy in the description of multi-electron dynamics in long-wavelength high-intensity lasers. The TD-CASSCF method is gauge invariant [37] and size extensive [38]. The fully correlated active space enables an accurate description of ionization processes including multichannel and multi-electron effects while dynamical-core orbitals efficiently account for the field-induced core polarization. More approximate and thus computationally even less demanding methods have also been developed [39–41], such as the time-dependent occupation-restricted multiple active-space (TD-ORMAS) method [41]. See Ref. [37] for a broad review of *ab initio* methods for multi-electron dynamics.

This paper reports on an efficient fully 3D implementation of the TD-CASSCF method for atoms in the field of a linearly polarized laser pulse. Simulations for long-wavelength high-intensity pulses involve a large simulation volume and high spatial resolution to represent the electronic motion with large quiver amplitudes and high kinetic energy, requiring a very large number K of basis functions (or equivalently, grid points) for expanding the orbital functions. We reduce the resulting computational cost and harness the advantages of the TD-CASSCF method by introducing a gauge-invariant description of the frozen-core subspace allowing a velocity-gauge simulation, which is known to be superior to the length gauge treatment for strong field phenomena [42, 43]. Our implementation employs a spherical harmonics expansion of orbitals with the radial coordinate discretized by a finite-element discrete variable representation (FEDVR) [44–47]. For the computationally most costly operation, the evaluation of the mean field, we use a Poisson solver thereby achieving linear scaling with K. A split-operator propagator is developed with an efficient implicit method for *stiff* derivative operators which drastically stabilizes the temporal propagation of orbitals. Combining these techniques makes it possible to take full advantage of the TD-CASSCF method and permits benchmark calculations for atoms. We present the HHG spectra for He, Be, and Ne atoms induced by an intense NIR laser pulse and explore the effect of the electron correlation. Our results are converged with respect to the spatial and temporal discretization. This paper is organized as follows. In Sec. II, we present the equations of motion (EOMs) for the TD-CASSCF method and introduce a gauge-invariant frozen-core treatment. Our implementation of the TD-CASSCF method for atomic systems is described in Sec. III, and numerical applications are described in Sec. IV. Section V concludes this work and discusses future prospects. In order to improve the readability of the manuscript, we have moved a considerable amount of technical details to Appendices A to E. Hartree atomic units are used throughout unless otherwise noted.

II. METHOD

A. The system Hamiltonian

We consider an atom with N electrons exposed to a laser field linearly polarized in the z direction. The Hamiltonian reads

$$H = \sum_{i=1}^{N} h(\boldsymbol{r}_i, \boldsymbol{p}_i, t) + \sum_{i=1}^{N} \sum_{j>i} U(\boldsymbol{r}_i, \boldsymbol{r}_j) \tag{2}$$

where $\boldsymbol{r}_i$ and $\boldsymbol{p}_i = -i\boldsymbol{\nabla}_i$ are the coordinate and canonical momentum of the electron i, with the one-body Hamiltonian

$$h(t) = h_0 + V_{\text{ext}}(t), \tag{3}$$

and the electron-electron interaction

$$U(\boldsymbol{r}_1, \boldsymbol{r}_2) = \frac{1}{r_{12}} = \frac{1}{|\boldsymbol{r}_1 - \boldsymbol{r}_2|}. \tag{4}$$

The atomic Hamiltonian h_0 and the laser-electron interaction V_{ext} within the dipole approximation either in the length gauge (LG) or in the velocity gauge (VG) are given by

$$h_0(\boldsymbol{r}, \boldsymbol{p}) = \frac{1}{2}p^2 + V_0(\boldsymbol{r}), \;\; V_0(\boldsymbol{r}) = -\frac{Z}{r} \tag{5}$$

$$V_{\text{ext}}^{\text{LG}}(\boldsymbol{r}, t) = E(t)z, \tag{6a}$$

$$V_{\text{ext}}^{\text{VG}}(\boldsymbol{p}, t) = A(t)p_z, \tag{6b}$$

where V_0 is the nuclear potential with Z being the atomic number, and $E(t)$ and $A(t) = -\int E(t)dt$ are the laser electric field and the vector potential, respectively. We will use the second-quantized operators $\hat{h}$, $\hat{U}$, and $\hat{H}$, etc., corresponding to those defined in real space in Eqs. (2) to (6). Explicit expressions for the operators in second quantization are given in Appendix A.

B. TD-CASSCF method

In the TD-CASSCF method [35], the n occupied orbitals are separated into n_{c} doubly occupied core orbitals $\{\psi_i : i = 1, 2, \cdots, n_{\text{c}}\}$ and n_{a} active orbitals $\{\psi_t : t = n_{\text{c}} + 1, n_{\text{c}} + 2, \cdots, n\}$, with $n = n_{\text{c}} + n_{\text{a}}$. The core orbitals can be further decomposed into n_{fc} FC orbitals and n_{dc} DC orbitals, with $n_{\text{c}} = n_{\text{fc}} + n_{\text{dc}}$. Then the N-electron wave function is given by

$$\Psi_{\text{CAS}} = \hat{A}\left[\Phi_{\text{fc}}\Phi_{\text{dc}} \sum_I \Phi_I C_I\right], \tag{7}$$

where $\hat{A}$ is the antisymmetrization operator, $\Phi_{\rm fc}$ and $\Phi_{\rm dc}$ are the closed-shell determinants constructed with FC and DC orbitals, respectively, and $\{\Phi_I\}$ are the determinants formed by active orbitals. Compared to stationary CASSCF calculations the required size of the active space in TD-CASSCF is, in general, larger due to the inclusion of dynamical excitation processes. Therefore, compared to CASSCF calculations TD-CASSCF is limited to smaller systems. Both methods have in common that the total number of configurations is limited by the available computer memory.

In the following we will denote the level of the CAS approximation employed in $\Psi_{\rm CAS}$ by the integer triple $(n_{\rm fc}, n_{\rm dc}, n_{\rm a})$ with $n_{\rm fc}+n_{\rm dc}+n_{\rm a}=n$. The MCTDHF method corresponds to the special case $(0,0,n)$. As the formulation of the TD-CASSCF method involves different classes of orbitals, we introduce for clarity specific index sets: for core orbitals we will use $\{i,j\}$, for active orbitals $\{t,u,v,w,x\}$ and for arbitrary orbitals (core and active) $\{o,p,q,r,s\}$. The FC and DC orbitals are distinguished explicitly only when necessary.

The equations of motion (EOMs) for the TD-CASSCF method has been derived based on the time-dependent variational principle [48–50], where the following action integral S,

$$S = \int dt \langle\Psi|\hat{H} - i\frac{\partial}{\partial t}|\Psi\rangle, \tag{8}$$

is required to be stationary, i.e, $\delta S = 0$ for the variation of orbitals $\{\psi_p\}$ and CI coefficients $\{C_I\}$. The form of the resulting EOMs is not unique but can be written in various equivalent ways (see Appendix B for further details). Here we present the EOMs in the form particularly well-suited for the split-operator method applied below. The EOMs for the CI coefficients read

$$i\dot{C}_I = \sum_J \langle\Phi_I|\hat{U}|\Phi_J\rangle C_J, \tag{9a}$$

and the EOMs of the orbitals are given by

$$i|\dot{\psi}_p\rangle = \hat{h}|\psi_p\rangle + \hat{Q}\hat{F}|\psi_p\rangle + \sum_q |\psi_q\rangle R^q_p, \tag{9b}$$

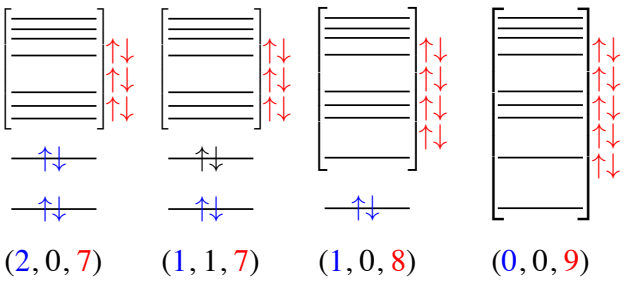

FIG. 1. Illustration of the TD-CASSCF concept for a 10-electron system with 9 occupied orbitals. The up and down arrows represent electrons decomposed into FC electrons (blue), DC electrons (black), and active electrons (red). The horizontal lines represent occupied orbitals, classified into doubly occupied FC and DC orbitals and active orbitals (bracketed). Three examples, (2,0,7), (0,1,8), and (0,0,9), correspond to the methods used for the Ne atom in Sec. IV C.

where $\hat{Q} = 1 - \sum_p |\psi_p\rangle\langle\psi_p|$ is the projector onto the orthogonal complement of the occupied orbital space. The operator $\hat{F}$ is defined by

$$\hat{F}|\psi_p\rangle = \sum_{oqsr} (D^{-1})^o_p P^{qs}_{or} \hat{W}^r_s |\psi_q\rangle, \tag{10}$$

where D and P are the one- and two-electron reduced density matrix (RDM), respectively (see Ref. [35] for their definition and the simplification due to the core-active separation), and

$$W^p_q(\boldsymbol{r}_1) = \int d\boldsymbol{r}_2 \frac{\psi^*_p(\boldsymbol{r}_2)\psi_q(\boldsymbol{r}_2)}{|\boldsymbol{r}_1 - \boldsymbol{r}_2|}. \tag{11}$$

is the matrix element for the Coulomb interaction. The matrix element R^q_p,

$$R^q_p \equiv i\langle\psi_q|\dot{\psi}_p\rangle - h^q_p \tag{12}$$

determines the components of the time derivative of orbitals in the subspace spanned by the occupied orbitals. The elements within one subspace, i.e., R^i_j and R^u_t, can be arbitrary Hermitian matrix elements and are set to zero $R^i_j = R^u_t = 0$ in the present implementation [35]. Elements between the core and active space are given by [35],

$$R^t_i = \sum_u (2-D)^{-1}_{tu} \left(2F^u_i - \sum_v D^u_v F^{i*}_v\right), \tag{13}$$

where $F^p_q = \langle\psi_p|\hat{F}|\psi_q\rangle$. The explicit solution of this set of EOMs (Eq. 9) in a spherical basis will be discussed below.

One important aspect of the TD-CASSCF method to be addressed is the preservation of gauge invariance. While the MCTDHF method is gauge invariant from the outset, the inequivalent treatment of frozen-core and active orbitals within the TD-CASSCF method requires the explicit introduction of gauge phases.

Previously [35, 41], the FC orbitals were identified with the field-free orbitals. This choice is justified only for the length gauge (LG). In order to render the TD-CASSCF gauge-invariant and to allow for the use of the numerically convenient velocity gauge (VG) we introduce gauge-dependent frozen-core orbitals as

$$|\psi_i(t)\rangle = \begin{cases} |\psi_i(0)\rangle & \text{(LG)} \\ e^{-iA(t)z}|\psi_i(0)\rangle & \text{(VG)} \end{cases} \quad (i \in \text{FC}). \tag{14}$$

Correspondingly the matrix element (Eq. 12)

$$R^p_i = (R^i_p)^* = \begin{cases} -h^p_i & \text{(LG)} \\ -h^p_i - E(t)z^p_i & \text{(VG)} \end{cases}, \tag{15}$$

where $i \in$ FC and $z^p_i = \langle\psi_p|z|\psi_i\rangle$.

III. IMPLEMENTATION FOR MANY-ELECTRON ATOMS

A. Spherical-FEDVR basis

In our implementation of the TD-CASSCF method for many-electron atoms we adopt the so called spherical-FEDVR

basis functions,

$$\chi_{klm}(r,\theta,\phi) = \frac{1}{r} f_k(r) Y_{lm}(\theta,\phi), \tag{16}$$

where (r,θ,ϕ) are the spherical coordinates of $\boldsymbol{r}$, Y_{lm} is a spherical harmonic, and $f_k(r)$ are normalized radial-FEDVR basis functions [44, 45]. We divide the radial coordinate $[0, R_{\max}]$ into $K_{\rm FE}$ elements with each element supporting $K_{\rm DVR}$ local DVR functions. The radial coordinate is thus discretized into $K_{\rm rad} = K_{\rm FE}K_{\rm DVR} - (K_{\rm FE} - 1)$ grid points $\{r_k\}$ (the term $K_{\rm FE}-1$ takes into account the bridge functions [44, 45] used for boundaries of neighboring finite elements), with integration weights $\{w_k^{\rm rad}\}$ such that

$$f_k(r_{k'}) = \frac{\delta_{kk'}}{\sqrt{w_k^{\rm rad}}}, \tag{17}$$

and $r_1 = 0$, $r_{K_{\rm rad}} = R_{\max}$ (For further details, see Refs. [32, 44, 45]).

We use m-adapted orbitals with fixed magnetic quantum number m_p (see Appendix C). Thus, we expand ψ_p as

$$\psi_p(r,\theta,\phi,t) = \sum_{k=2}^{K_{\rm rad}-1} \sum_{l=0}^{L_{\max}} \chi_{klm_p}(r,\theta,\phi) \varphi_p^{kl}(t), \tag{18}$$

where the first and last FEDVR basis function are removed to ensure the boundary condition that orbitals vanish at both edges of the simulation box [45]. The spherical harmonics expansion is truncated after the maximum angular momentum $L_{\max}$. In total, the number of basis functions in Eq. (18) is $K = (K_{\rm rad} - 2)(L_{\max} + 1)$.

The vector $\boldsymbol{\varphi}_p$ of expansion coefficients with elements φ_p^{kl} is our working variable, with which the orbital EOM Eq. (9b) reduces to a matrix equation,

$$i\frac{d}{dt}\boldsymbol{\varphi}_p = \boldsymbol{h}\boldsymbol{\varphi}_p + \boldsymbol{Q}\boldsymbol{F}\boldsymbol{\varphi}_p + \sum_q \boldsymbol{\varphi}_q R_p^q. \tag{19}$$

Here, the matrices $\boldsymbol{Q}$, $\boldsymbol{h}$, and $\boldsymbol{F}$ represent operators $\hat{Q}$, $\hat{h}$, and $\hat{F}$ in the spherical-FEDVR basis [Eq. (16)]. Explicit expressions for matrix elements of the one-electron operator, $\boldsymbol{h} = \boldsymbol{h}_0 + \boldsymbol{V}_{\rm ext}$, are given in Appendix E. For the electron-electron interaction, we use the multipole expansion

$$\frac{1}{r_{12}} = \sum_{l=0}^{L_{\rm ee}} \sum_{m=-l}^{l} \frac{4\pi}{2l+1} \frac{r_<^l}{r_>^{l+1}} Y_{lm}(\theta_1,\phi_1) Y_{lm}^*(\theta_2,\phi_2), \tag{20}$$

where $r_>$ ($r_<$) is the greater (smaller) of r_1 and r_2, $L_{\rm ee}$ is the highest multipole rank reached, $L_{\rm ee} \le 2L_{\max}$, for the basis expansion of orbitals with $l \le L_{\max}$. The two-electron part $\boldsymbol{F}\boldsymbol{\varphi}_p$ is evaluated by (i) first calculating the mean field, Eq. (11), by solving Poisson's equation,

$$\nabla^2 W_q^p(\boldsymbol{r}) = -4\pi \psi_p^*(\boldsymbol{r})\psi_q(\boldsymbol{r}), \tag{21}$$

in the spherical-FEDVR basis of Eq. (16) [32, 45], and (ii) performing the integrals weighted with RDMs through Eq. (10) in the two-dimensional grid representation of coordinates (r,θ) with the known ϕ dependence analytically integrated out (see Appendix E for further details).

B. Split operator propagator

The orbital EOM Eq. (19) consists of both the linear (i.e., independent of orbital functions and CI coefficients) term $\boldsymbol{h}$ and the nonlinear terms containing dependencies on the orbitals and the CI coefficients. Moreover, the linear part contains the stiff spatial-derivative operators while the nonlinear part is non-stiff. We therefore introduce an effective split-operator algorithm that uses adapted propagators for $\boldsymbol{h}$ and the nonlinear part. We use a second-order split method [28, 51, 52], in which the propagation for the time interval $[t, t+\delta t]$ is performed as follows. First we solve the linear equation

$$\frac{d}{dt}\boldsymbol{\varphi}_p = -i\boldsymbol{h}(t)\boldsymbol{\varphi}_p, \tag{22}$$

for $[t, t+\delta t/2]$ with initial values $\{\boldsymbol{\varphi}_p(t)\}$ to obtain $\{\boldsymbol{\varphi}_p'\}$, with CI coefficients kept fixed, $C_I' = C_I(t)$. Then Eqs. (9), for the nonlinear part and the CI coefficients are solved for $[t, t+\delta t]$ with initial values $\{\boldsymbol{\varphi}_p', C_I'\}$ to obtain $\{\boldsymbol{\varphi}_p'', C_I''\}$. Finally Eq. (22) is solved again for $[t+\delta t/2, t+\delta t]$ with initial values $\{\boldsymbol{\varphi}_p''\}$ and CI coefficients kept fixed to obtain $\{\boldsymbol{\varphi}_p(t+\delta t), C_I(t+\delta t) = C_I''\}$. For the stiff Eq. (22) we adopt the Crank-Nicolson method,

$$\boldsymbol{\varphi}_p(t+\delta t/2) = \frac{1 - i\boldsymbol{h}(t+\delta t/4)\delta t/4}{1 + i\boldsymbol{h}(t+\delta t/4)\delta t/4}\boldsymbol{\varphi}_p(t). \tag{23}$$

The right hand side is evaluated by the matrix iteration method [42], in which the inverse operator is expanded as

$$\begin{aligned}(1 + i\boldsymbol{h}\delta t')^{-1} &= \left\{(1 + i\boldsymbol{h}_0\delta t')\left(1 + \frac{i\boldsymbol{V}_{\rm ext}\delta t'}{1 + i\boldsymbol{h}_0\delta t'}\right)\right\}^{-1} \\ &= \left(1 + \frac{i\boldsymbol{V}_{\rm ext}\delta t'}{1 + i\boldsymbol{h}_0\delta t'}\right)^{-1} \frac{1}{1 + i\boldsymbol{h}_0\delta t'} \\ &= \sum_{m=0}^{\infty} \left(-\frac{i\boldsymbol{V}_{\rm ext}\delta t'}{1 + i\boldsymbol{h}_0\delta t'}\right)^m \frac{1}{1 + i\boldsymbol{h}_0\delta t'},\end{aligned} \tag{24}$$

with $\delta t' = \delta t/4$. This defines an iterative procedure,

$$\boldsymbol{\varphi}_p(t+\delta t/2) \approx \sum_{j=0}^{N_{\rm itr}} \boldsymbol{f}_j, \tag{25}$$

$$(1 + i\boldsymbol{h}_0\delta t')\,\boldsymbol{f}_0 = (1 - i\boldsymbol{h}\delta t')\,\boldsymbol{\varphi}_p(t), \tag{26a}$$

$$(1 + i\boldsymbol{h}_0\delta t')\,\boldsymbol{f}_j = -i\boldsymbol{V}_{\rm ext}\delta t'\,\boldsymbol{f}_{j-1} \quad (j \ge 1). \tag{26b}$$

This method has been found to be quite efficient for ionization dynamics of atomic hydrogen under the presence of an intense, long-wavelength laser field [43]. Since $\boldsymbol{h}_0$ is diagonal in the angular momentum basis and very sparse in the radial FEDVR basis (see Appendix E), the systems of linear equations (26) can be solved with computational cost that scales linearly with respect to K. For the nonlinear, but nonstiff part on the right-hand side of Eq. (9b), we use the fourth-order Runge-Kutta propagator.

IV. NUMERICAL RESULTS FOR HHG IN MANY-ELECTRON ATOMS

In this section, we present numerical applications of the implementation of the TD-CASSCF method to many-electron atoms described in the previous section. In all simulations reported below, the initial state is taken as the ground state obtained through imaginary time propagation of the EOMs. We assume a laser field of the following form:

$$E(t) = E_0 \sin(\omega_0 t) \sin^2\left(\pi \frac{t}{\tau}\right), \quad 0 \le t \le \tau, \qquad (27)$$

with total duration τ, peak intensity $I_0 = E_0^2$, wavelength $\lambda = 2\pi/\omega_0$, and period $T = 2\pi/\omega_0$. For all simulations presented a uniform finite element length of $d_{\rm FE}$ is used. The code allows, however, variable element sizes for the radial-FEDVR basis, if needed.

A. Helium

First we simulate a helium atom subject to a field of 400 nm wavelength, 4.0×10^{14} W/cm^2 intensity, and total duration of 12 periods T of the optical field ($\tau = 12T$). For this system, a direct exact numerical solution of the time-dependent Schrödinger equation (TDSE) is possible and serves as a benchmark for the present TD-CASSCF code. Note that for this two-electron system, the TD-CASSCF method reduces to TDHF for the orbital choice $(n_{\rm fc} = 0, n_{\rm dc} = 0, n_{\rm a} = 1)$ or to the MCTDHF method for $(n_{\rm fc} = 0, n_{\rm dc} = 0, n_{\rm a} > 1)$. The TDSE simulations are performed using the code developed at Vienna University of Technology [17, 18, 47], in which the six-dimensional two electron wave function is expanded with coupled spherical harmonics, and the radial coordinates are discretized with a FEDVR basis. The code is highly optimized and massively parallelized enabling the large scale simulations as presented below. Here we aim at a rigorous comparison between the TD-CASSCF (or MCTDHF) method and the TDSE results under otherwise identical simulation conditions.

We use the radial-FEDVR basis with $K_{\rm FE} = 80$, $d_{\rm FE} = 4.0$, $K_{\rm DVR} = 11$, and $R_{\rm max} = 320$, and spherical harmonics expansions with $L_{\rm max} = L_{\rm ee} = 13$. To avoid a reflection at the simulation box boundary, orbital functions on the radial grid points $r_k > 256$ are masked after each time propagation by a $\cos^{1/4}$ function. Both TDSE and MCTDHF simulations employ the velocity gauge. Several time-step sizes are tested (from 20000 to 40000 steps per cycle) for the MCTDHF method. The TDSE simulation uses the short iterative Lanczos propagator with self-adaptive time-step sizes. We

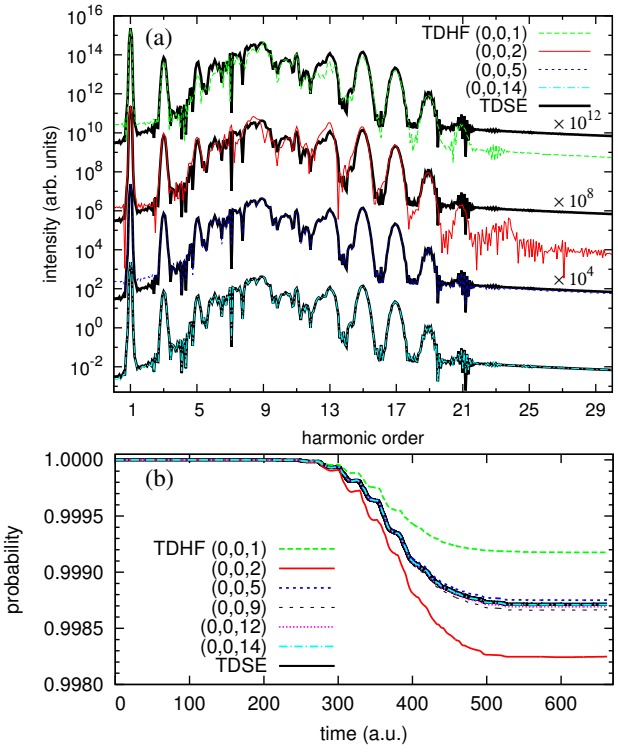

FIG. 2. (a) High harmonic generation spectrum of a He atom exposed to a visible laser pulse with a wavelength of 400 nm and an intensity of 4×10^{14} W/cm^2. (b) The probability to find both electrons within a sphere of radius $R_0 = 20$ a.u. Results of the TD-CASSCF (or MCTDHF) method with different number of active orbitals $(0, 0, n)$ are compared to the result of the exact TDSE method. $(0, 0, 1)$ corresponds to TDHF.

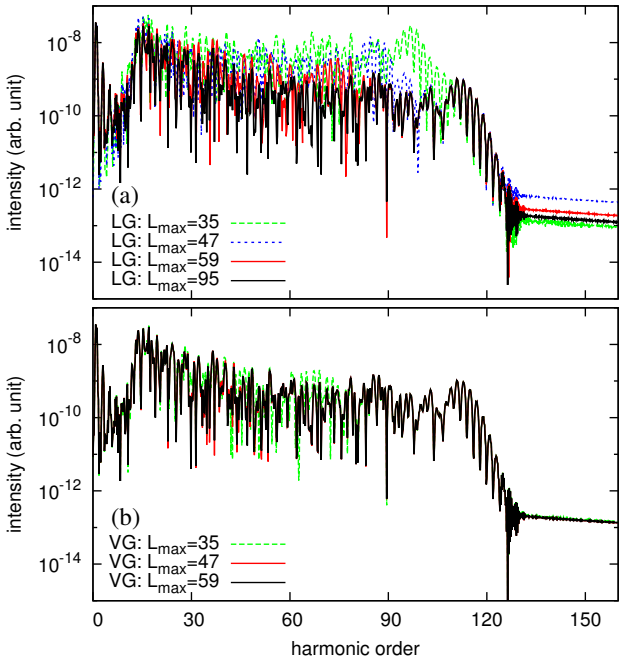

FIG. 3. HHG spectra of He exposed to an IR laser pulse with a wavelength of 800 nm and an intensity of 8×10^{14} W/cm^2. Results for (a) length gauge (LG) and (b) velocity gauge (VG) simulations with the TD-CASSCF (or MCTDHF) method with fixed orbital indices $(0, 0, 5)$ as a function of maximum angular momentum $L_{\rm max}$ in the orbital expansion.

have carefully checked that the spatial and temporal resolutions used are sufficient for reaching fully converged results both for TDSE and MCTDHF simulations.

The HHG spectra [Fig. 2 (a)] calculated as the modulus squared of the Fourier transform of the dipole acceleration [using the Ehrenfest expression Eq. (29b) below] display increasing agreement between MCTDHF and TDSE results as the number of orbitals is increased. The MCTDHF with $n \geq 5$ essentially reproduces the TDSE spectrum, and in particular, with $n = 14$ the agreement is almost perfect over a dynamical range of 5 orders of magnitude. Likewise, the probability of finding both two electrons inside a sphere of radius $R_0 = 20$ a.u. (referred to as survival probability hereafter) measuring the temporal evolution of the complement to ionization or formation of Rydberg states [Fig. 2 (b)] yields close agreement for $(0, 0, n)$ with $n > 2$. For $n = 14$ the MCTDHF results become indistinguishable from TDSE. Note, however, significant differences to the TDHF limit pointing to the crucial role of correlations included in the MCTDHF method but neglected by TDHF.

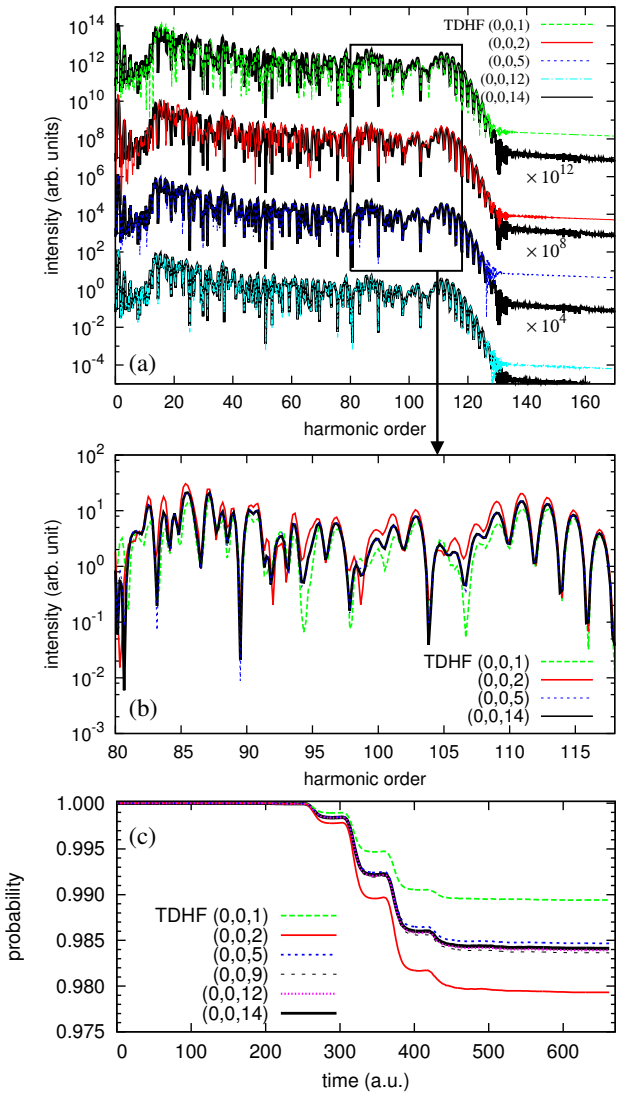

FIG. 4. (a) HHG spectra of He exposed to an IR laser pulse with a wavelength of 800 nm and an intensity of 8×10^{14} W/cm^2, (b) close-up of the region between the 80$^{\text{th}}$ and the 118$^{\text{th}}$ harmonic, and (c) the probability to find both electrons within a sphere of radius $R_0 = 20$ a.u. Results of the TD-CASSCF (or MCTDHF) method are obtained with different number n of active orbitals $(0, 0, n)$ and maximum angular momentum $L_{\max} = 59$.

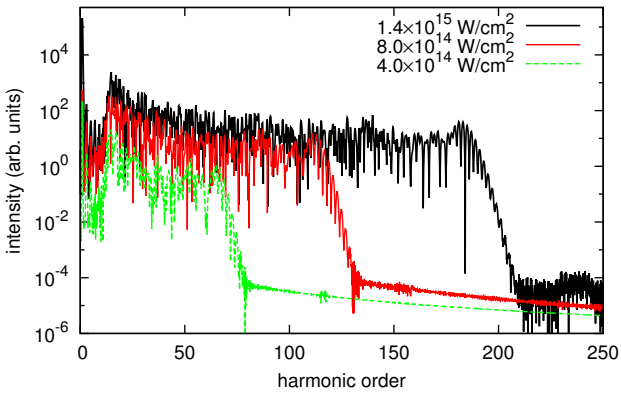

FIG. 5. HHG spectra of He exposed to an IR laser pulse with a wavelength of 800 nm and varying intensities of 4, 8, and 14×10^{14} W/cm^2, obtained with the TD-CASSCF (or MCTDHF) method with orbital indices $(0, 0, 14)$ and maximum angular momentum of $L_{\max} = 71$.

Next we proceed to the convergence test as a function of $L_{\max}$ $(= L_{\text{ee}})$ for both LG and VG. We consider now the longer-wavelength and higher-intensity regime ($\lambda = 800$ nm, $I_0 = 8\times10^{14}$ W/cm^2, and $\tau = 6T$), for which convergence of the exact TDSE code is still difficult to achieve. We reduce the FEDVR-element size to $d_{\text{FE}} = 2.0$ in order to improve the representation of higher-energy electrons and fix the orbital set to $(0, 0, 5)$. The HHG spectrum converges for VG (Fig. 3) much faster than for LG. While in the VG $L_{\max} = 47$ suffices to reach overall good agreement with the fully converged results, angular momenta up to $L_{\max} \approx 90$ are needed in the LG for comparable accuracy. The convergence of the survival probability and of the harmonic spectrum as a function of n (Fig. 4) is fairly rapid. Slight underestimation ($n = 1$) and overestimation ($n = 2$) of harmonic intensities as seen [Fig. 4 (b)] in the upper plateau region, are closely related to the underestimation ($n = 1$) and overestimation ($n = 2$) of the ionization [Fig. 4 (c)].

Figure 5 presents HHG spectra for the wavelength 800 nm and three different intensities, 4, 8, and 14×10^{14} W/cm^2. The results are converged, up to the cutoff frequencies, in radial resolution ($d_{\text{FE}} = 2$), angular resolution ($L_{\max} = L_{\text{ee}} = 71$), temporal resolution (20000 steps per cycle), and number of orbitals ($n = 14$). We stress the importance of the VG implementation, with LG the convergence with respect to $L_{\max}$ was hardly reachable for the highest intensity. Finally, we compare the converged TD-CASSCF survival probability with predictions of the widely adopted Ammosov-Delone-Krainov (ADK) [53] and Perelomov-Popov-Terentev (PPT)

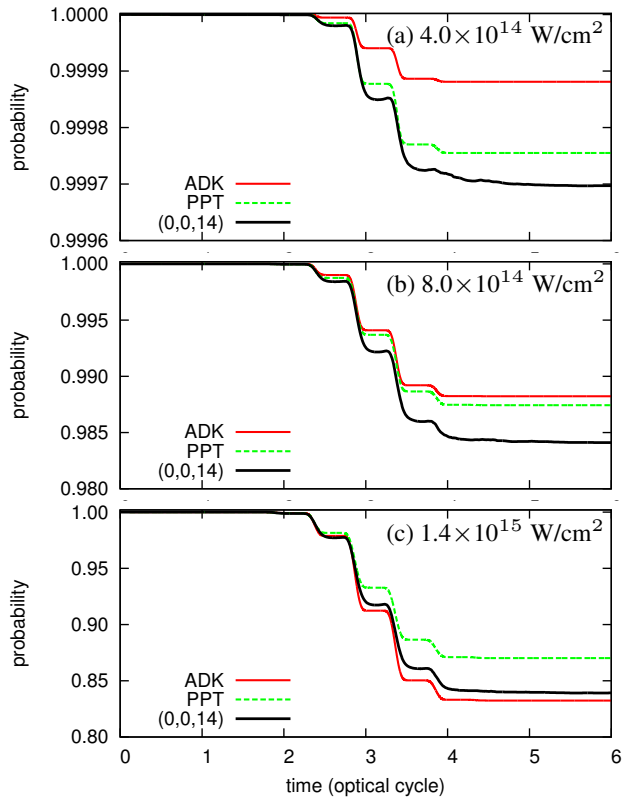

FIG. 6. Time evolution of the survival probability of helium obtained with TD-CASSCF with 14 active orbitals $(0, 0, 14)$ as well as ADK and PPT with the same computational condition as for Fig. 5, a wavelength of 800 nm and intensities of (a) 4, (b) 8, and (c) 14×10^{14} W/cm^2. For the survival probabilities to match those of TD-CASSCF the ADK rates must be scaled by 2.55, 1.35, and 0.96 for the three intensities in ascending order. The analogous factors for the PPT rates are 1.24, 1.27, and 1.24. The ADK and PPT probabilities are shifted in time to take into account the time required for an ejected electron to propagate classically to $R_0 = 20$ a.u.

models [54] (see Fig. 6). The ADK and PPT probabilities are calculated by integrating over the temporal profile of the laser electric field. The ADK model fails to reproduce the intensity dependence of the survival probability underestimating the ionization probability at moderate intensity while approaching the TD-CASSCF result at high intensity. The PPT model, on the other hand, consistently underestimates the ionization by a nearly constant factor independent of the intensity. The present simulation for helium demonstrates the accuracy of the present TD-CASSCF implementation by both the excellent agreement with the TDSE (where available) and the convergence with respect to all parameters characterizing the CASSCF orbital expansion.

B. Beryllium

Beryllium is the first test case for the decomposition into frozen- and dynamical-core orbitals as well as active orbitals available in the TD-CASSCF method. Extraction of the harmonic spectrum via the expectation value of the dipole acceleration using the Ehrenfest theorem requires additional care in the presence of frozen orbitals. Using the Ehrenfest theorem and the canonical commutation relation $[\hat{z}, \hat{p}_z] = i$, the dipole moment, dipole velocity, and dipole acceleration are given by

$$\langle \hat{z} \rangle = \langle \Psi | \hat{z} | \Psi \rangle, \tag{28}$$

$$\frac{d}{dt}\langle \hat{z} \rangle = \langle \Psi | \hat{p}_z | \Psi \rangle, \tag{29a}$$

and

$$\frac{d^2}{dt^2}\langle \hat{z} \rangle = -\langle \Psi | \left(\frac{\partial \hat{V}_0}{\partial z} + \frac{\partial \hat{V}_{\rm ext}}{\partial z} \right) | \Psi \rangle, \tag{29b}$$

respectively. Equations (28) and (29) hold for the solutions $|\Psi\rangle$ of the TDSE as well as the TD-MCSCF. However, in the presence of frozen orbitals, Eqs. (29) must be modified to (for details see Appendix D),

$$\frac{d}{dt}\langle \hat{z} \rangle_{\rm fc} = \langle \Psi | \hat{p}_z | \Psi \rangle + \Delta(\dot{z}), \tag{30a}$$

$$\frac{d^2}{dt^2}\langle \hat{z} \rangle_{\rm fc} = -\langle \Psi | \left(\frac{\partial \hat{V}_0}{\partial z} + \frac{\partial \hat{V}_{\rm ext}}{\partial z} \right) | \Psi \rangle + \Delta(\dot{p}_z), \tag{30b}$$

where the additional term Δ is defined by Eq. (D5). The appearance of this correction term in the presence of frozen orbitals can be qualitatively easily understood as follows: Focusing at the moment on the equations for the force [Eqs. (29b), (30b)], the dipole acceleration is given by the expectation value $\langle -\frac{\partial H}{\partial z} \rangle$ of the total force on the electronic system. It consists of the laser acting on the active electrons, $f_{\rm la}$, the laser acting on the core electrons, $f_{\rm lc}$, the nuclear force acting on active, $f_{\rm na}$, and core electrons, $f_{\rm nc}$, and the inter-electronic forces, $f_{\rm ac}$ and $f_{\rm ca}$. With the action-reaction law, $f_{\rm ac} = -f_{\rm ca}$, the total force becomes

$$f = (f_{\rm na} + f_{\rm nc}) + (f_{\rm la} + f_{\rm lc}), \tag{31}$$

which corresponds to the Ehrenfest expression Eq. (29b). However, for the case of frozen-core orbitals, we have to include an additional "binding force" $f_{\rm b}$ to render the frozen-core immobile,

$$f = (f_{\rm na} + f_{\rm nc}) + (f_{\rm la} + f_{\rm lc}) + f_{\rm b}. \tag{32}$$

The "binding force" $f_{\rm b}$ must cancel all forces acting on frozen-core electrons,

$$f_{\rm b} = -f_{\rm nc} - f_{\rm lc} - f_{\rm ac}. \tag{33}$$

Consequently, the effective force in the presence of a frozen core becomes

$$f_{\rm eff} = (f_{\rm na} + f_{\rm ca}) + f_{\rm la}, \tag{34}$$

i.e., the inter-electronic force no longer cancels. The correction term $\Delta(\dot{p}_z)$ represents the binding force $f_{\rm b}$ [see

Eq. (D9)], and Eq. (30b) is the proper quantum expression for the effective force [Eq. (34)]. Use of the correct expression Eq. (30b) is essential; otherwise the missing binding force would lead to an incorrect evaluation of the dipole acceleration. This is illustrated in Fig. 7 showing the time evolutions of (a) the dipole moment, (b) the dipole velocity, and (c) the dipole acceleration of Be irradiated by an intense NIR laser pulse ($\lambda = 800$ nm, $I_0 = 4.0 \times 10^{14}$ W/cm^2, and $\tau = 3T$) calculated with the TD-CASSCF method either with the DC $[(n_{\rm fc}, n_{\rm dc}, n_{\rm a}) = (0, 1, 5)]$ or the FC $[(n_{\rm fc}, n_{\rm dc}, n_{\rm a}) = (1, 0, 5)]$ treatment of the initial $1s$ orbital. For the FC case, we compare the standard Ehrenfest expression, Eq. (29), and the one with the correction term, Eq. (30). The dipole moment, velocity, and acceleration obtained with DC and FC simulations [Eqs. (30)] agree very well with each other, suggesting that FC is a good approximation for beryllium. The FC velocities calculated with Eq. (29) and Eq. (30) are similar to each other, reflecting the fact that $\Delta(\dot{z}) \approx 0$ as demonstrated in Appendix D. However, the FC acceleration evaluated by the standard Ehrenfest expression, Eq. (29b), fails. Only when the correction term $\Delta(\dot{p}_z)$ is included [Eq. (30b)] excellent agreement between the FC and DC treatment is achieved for the dipole acceleration [Fig. 7 (c)], and therefore the HHG spectrum [Fig. 8 (a)] calculated as the modulus squared of the Fourier transform of the dipole acceleration.

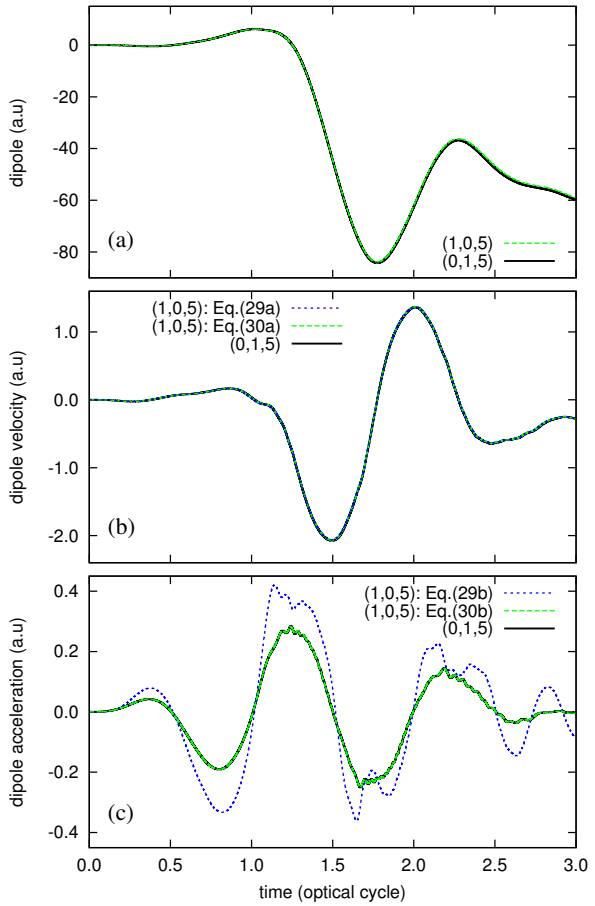

FIG. 7. Time evolution of (a) the dipole moment, (b) the dipole velocity, and (c) the dipole acceleration of Be exposed to an IR laser pulse with a wavelength of 800 nm and an intensity of 3.0×10^{14} W/cm^2, obtained with the TD-CASSCF method with one dynamical-core orbital $(n_{\rm fc}, n_{\rm dc}, n_{\rm a}) = (0, 1, 5)$ or one frozen-core orbital $(1, 0, 5)$ and a maximum angular momentum of $L_{\rm max} = 47$.

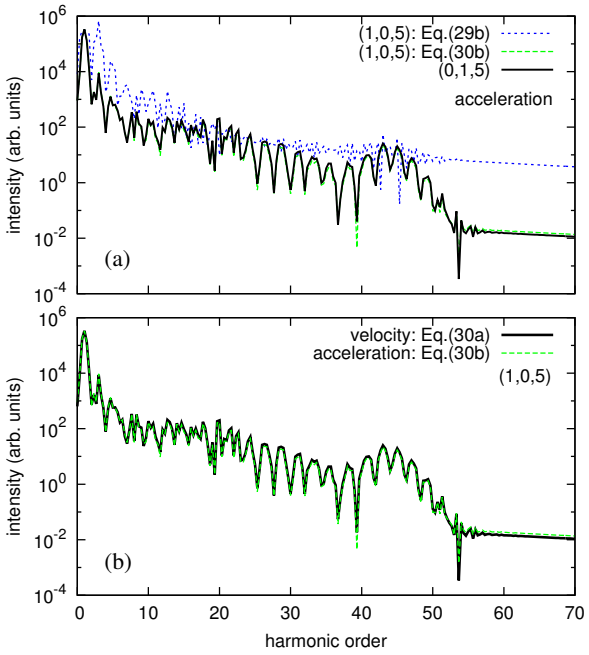

FIG. 8. The HHG spectra of Be for the same laser pulse and the simulation condition as those in Fig. 7. (a) The HHG spectra computed from the dipole acceleration using the active spaces $(n_{\rm fc}, n_{\rm dc}, n_{\rm a}) = (1, 0, 5)$ and $(0, 1, 5)$. (b) Comparison of the spectra computed from the dipole velocity and the dipole acceleration using the active space $(1, 0, 5)$.

The point to be emphasized is that it is not the FC approximation itself but the evaluation of the nonlinear response via the standard Ehrenfest expression, Eq. (29b), that fails. This observation has implications also for other approximation schemes in which the core is kept frozen, most notably for TDSE solutions of many-electron systems in the single-active electron (SAE) approximation. For example, Gordon *et al.* [55] have argued that one should use Eq. (31) [Eq. (10) of Ref. [55]] rather than Eq. (34) [equivalent to (the second time derivative of) Eq. (6) of Ref. [55]]. The present results suggest the opposite, i.e., that acceleration in the screened effective potential [Eq. (34)] rather than bare nuclear potential [Eq. (31)] should be used.

As a further confirmation for the validity of the modified Ehrenfest theorem [Eq. 30b] we find excellent agreement between HHG spectra obtained from the dipole acceleration [Eq. (30b)] and the dipole velocity [Eq. (30a)], when the latter is Fourier transformed after the numerical differentiation with respect to time [Fig. 8 (b)]. Moreover, this agreement demonstrates numerical convergence.

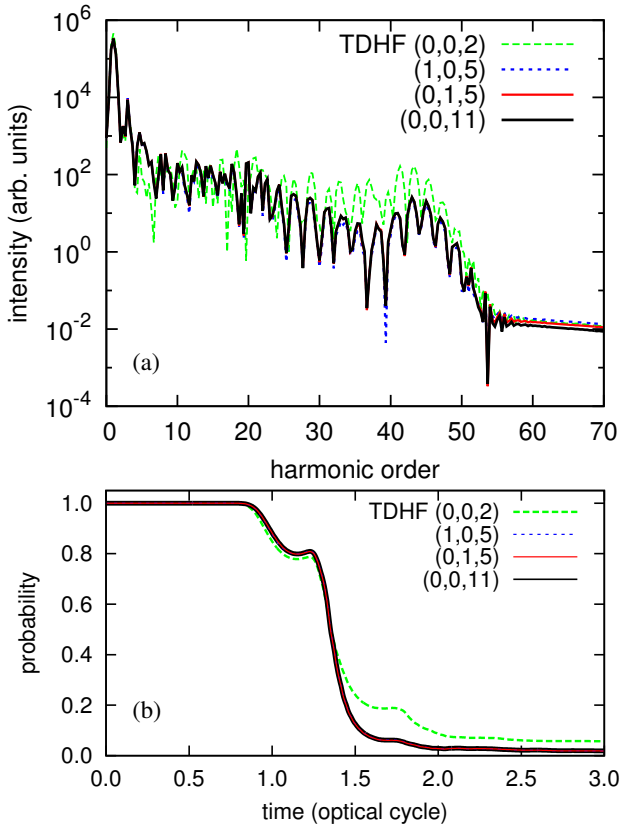

FIG. 9. (a) HHG spectra of Be exposed to an IR laser pulse with a wavelength of 800 nm and an intensity of 3×10^{14} W/cm^2. (b) Probability to find all electrons within a sphere of radius $R_0 = 20$ a.u. Results of TDHF and TD-CASSCF with $(n_{\rm fc}, n_{\rm dc}, n_{\rm a})$=$(0,0,2)$, $(1,0,5)$, $(0,1,5)$, and $(0,0,11)$.

The HHG spectrum as well as the survival probability of beryllium (Fig. 9) for the same laser parameters as in Fig. 7 indicate rapid convergence of the TD-CASSCF method as a function of the size of the active space. We have checked that the employed spherical-FEDVR basis ($d_{\rm FE} = 4, K_{\rm DVR} = 21, R_{\rm box} = 320$, and $L_{\rm max} = L_{\rm ee} = 47$) and the time-step size (20000 steps per cycle) are sufficient for convergence. Results for various active spaces $(n_{\rm fc}, n_{\rm dc}, n_{\rm a}) = (1,0,5)$, $(0,1,5)$, and $(0,0,11)$ closely agree with each other indicating convergence with respect to correlation. By contrast, the TDHF method which lacks correlation gives significant deviations. Unlike for helium where the TDHF underestimates HHG (Fig. 4) it overestimates HHG in beryllium (Fig. 9). This can be qualitatively easily understood as follows. In the strong-field regime and following the three-step model [56] the harmonic yield $P(\omega)$ is expected to scale with the product of the ionization rate at tunneling time $\sim |\dot{P}_0(t_i)|$ and the probability for finding the occupied ground state at recombination time $\sim P_0(t_r)$,

$$P(\omega) \propto |\dot{P}_0(t_i)| P_0(t_r). \tag{35}$$

In general, TDHF tends to underestimate the ionization rate $|\dot{P}_0(t)|$ and therefore overestimate the ground-state probability $\sim P_0(t)$ [57], as can be seen in Figs. 4 (c) and 9 (b). For the deeply bound helium electron (Fig. 4), $P_0(t) \approx 1$ holds for all t for intensities $I \lesssim 10^{14}$ W/cm^2. Thus, the ionization rate $|\dot{P}_0(t)|$ is the dominant factor in Eq. (35), leading to an underestimate of the harmonic intensity [Fig. 4 (c)]. On the other hand, for beryllium with a relatively weakly bound $2s$ valence electron, the atom experiences almost complete depletion of the ground state P_0 at $t > 1.5T$, which controls now the efficiency of harmonic emission. Since TDHF again largely overestimates P_0 especially at $t > 1.5T$ [Fig. 9 (b)] which is the relevant recombination time t_r contributing to the plateau and cut-off region of the harmonic spectrum, it now overestimates the harmonic intensity. This example nicely illustrates the importance to go beyond the mean-field level of the TDHF approximation (or TDDFT where the same trends can be observed).

C. Neon

Finally, we calculate the HHG spectrum of Ne subject to a laser field with $\lambda = 800$ nm, $I_0 = 8.0\times10^{14}$ W/cm^2, and $\tau = 3T$. We use the spherical-FEDVR basis with $d_{\rm FE} = 4.0$, $K_{\rm DVR} = 21$, and $L_{\rm max} = L_{\rm ee} = 47$. Simulations are performed in VG, and the HHG spectrum is calculated in the acceleration form. For this 10-electron system we apply the TD-CASSCF method for various active spaces with $(n_{\rm fc}, n_{\rm dc}, n_{\rm a}) = (2,0,7)$, $(1,0,8)$, and $(0,0,9)$. The 9 orbitals included are initially characterized as the atomic orbitals $1s$, $2s$, $2p_m$, $3s$, $3p_m$, with $m \in \{-1,0,1\}$. We consider either the $1s$ electrons to be frozen corresponding to $(1,0,8)$, or both $1s$ and $2s$ electrons to be frozen corresponding to $(2,0,7)$, or all electrons active $(0,0,9)$ (see Fig. 1). We obtain excellent agreement among all three active space configurations with a fixed total number of orbitals (Fig. 10) indicating that the electron dynamics governing HHG is dominated by the $2p$ electrons. For a convergence check with respect to correlation, we also performed a TD-CASSCF calculation with a larger number of active orbitals with frozen $1s$ orbital $(1,0,13)$. We find near-perfect agreement among all TD-CASSCF calculations. Only the TDHF calculation shows systematic deviations underestimating the harmonic intensity as was the case for helium (see Fig. 4). The TD-CASSCF method is key to systematically explore the inclusion of correlation effects. The CI dimension for the TD-CASSCF$(1,0,13)$ is about 1/8 ($\sim$ 500 thousands) of that for all active MCTDHF method ($\sim$ 4 million) with the same number of occupied orbitals. In addition, the FC approximation brings further computational efficiency: freezing the deepest bound $1s$ orbital improves the stability of the propagation over the duration of the laser pulse.

V. SUMMARY

We have presented an efficient 3D numerical implementation of the TD-CASSCF method for atoms subject to a linearly polarized strong laser pulse. It features (i) a gauge-invariant frozen-core approximation allowing velocity gauge

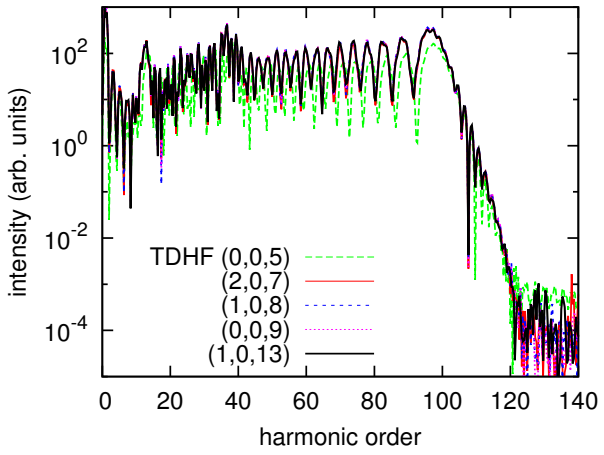

FIG. 10. HHG spectrum computed from the dipole acceleration of Ne driven by an IR laser pulse with $\lambda = 800$ nm, $I = 8.0\times10^{14}$ W/cm^2, obtained with TDHF and TD-CASSCF with $(n_{\rm fc}, n_{\rm dc}, n_{\rm a})$=$(0,0,5)$, $(2,0,7)$, $(1,0,8)$, $(0,0,9)$, and $(1,0,13)$. Except for TDHF all results coincide within the graphical resolution.

simulations suitable for high-field phenomena, (ii) an efficient evaluation of the mean field operator with the computational cost scaling linearly with the number of basis functions, and (iii) a split-operator method with a stable implicit propagator for the one-electron Hamiltonian. We have also derived and implemented the correction to the Ehrenfest expression the of dipole velocity and acceleration forms to be used with frozen-core orbitals.

We have applied the present theory to He, Be, and Ne atoms, and obtained survival probabilities and HHG spectra for intense NIR laser pulses, convergent with respect to spatial and temporal discretization, as well as the size of the active space. Our results indicate that the effect of correlation is relatively small for He, but significant for Be and Ne, which underlines the general importance of methods beyond the single-determinant TDHF approach. Correlation effects are expected to be even more prominent for processes explicitly involving motions of two or more electrons, such as nonsequential double ionization. For accurately treating multi-electron and correlation effects, high levels of radial and angular resolution of the orbitals are required. Otherwise such effects would be obscured by artifacts stemming from an insufficient resolution of the orbitals as demonstrated in the slow convergence of HHG spectrum of He with respect to the number of spherical harmonics (Fig. 3). The present efficient implementation allows to employ a large basis set (several thousands of radial grid points $K_{\rm rad}$ and a few hundred partial waves $L_{\rm max}$ are feasible on a single-node computer). Further improvement could be achieved by employing multi-scale resolution grids recently implemented for molecules [58]. For problems requiring active spaces larger than those realistically accessible with the TD-CASSCF method, promising lower-cost methods such as TD-ORMAS method [41] and two-particle reduced density matrix theory [59] will be considered in the future, for which the present gauge-invariant FC treatment and the efficient propagation scheme can be straightforwardly applied. These develpment will further extend the applicability to systems with a larger number of electrons and/or broader range of laser parameters, and will open the possibility of, e.g, *ab initio* simulations of XUV-NIR pump-probe experiments.

ACKNOWLEDGMENTS

We thank Othmar Koch for helpful discussions on propagation techniques and Johannes Feist for his work in the development of the TDSE helium code. This research is supported in part by Grant-in-Aid for Scientific Research (No. 25286064, 26390076, 26600111, and 16H03881) from the Ministry of Education, Culture, Sports, Science and Technology (MEXT) of Japan, and also by the Advanced Photon Science Alliance (APSA) project commissioned by MEXT. This research is also partially supported by the Center of Innovation Program from the Japan Science and Technology Agency, JST, and by CREST, JST, and by the FWF-special research programs F041-VICOM and F049-NEXTlite, the FWF DK Solids4fun, and the WWTF project MA14-002. The TDSE results have been achieved using the Vienna Scientific Cluster (VSC).

Appendix A: Second-quantization formulation

We briefly review the formulation of the TD-MCSCF [40, 41] and TD-CASSCF theories [35] within the framework of second quantization which allows for a compact presentation of the theory. Using fermionic creation and annihilation operators $\{\hat{a}_{\mu\sigma}, \hat{a}^\dagger_{\mu\sigma} : \sigma \in \uparrow,\downarrow\}$ which change the occupation of spin orbitals $\{\psi_\mu\} \otimes \{\uparrow,\downarrow\}$ with orthonormal spatial orbitals $\{\psi_\mu\}$, the system Hamiltonian, Eq. (2), can be rewritten as

$$\hat{H} = \hat{h} + \hat{U} \tag{A1}$$

$$= \sum_{\mu\nu} h^\mu_\nu \hat{E}^\mu_\nu + \frac{1}{2}\sum_{\mu\nu\gamma\lambda} U^{\mu\gamma}_{\nu\lambda}\hat{E}^{\mu\gamma}_{\nu\lambda}, \tag{A2}$$

where h^ν_μ and $U^{\nu\lambda}_{\mu\gamma}$ are matrix elements of the corresponding operators [see Eqs. (3) and (4)] , $\hat{E}^\mu_\nu = \sum_\sigma \hat{a}^\dagger_{\mu\sigma}\hat{a}_{\nu\sigma}$, and $\hat{E}^{\mu\gamma}_{\nu\lambda} = \sum_{\sigma\sigma'} \hat{a}^\dagger_{\mu\sigma}\hat{a}^\dagger_{\gamma\sigma'}\hat{a}_{\lambda\sigma'}\hat{a}_{\nu\sigma}$.

In the TD-MCSCF method, the full set of orbitals $\{\psi_\mu\}$ is classified as n occupied orbitals $\{\psi_p; p = 1, 2, \ldots, n\}$ and the remaining as virtual orbitals $\{\psi_a; a = n+1, n+2, \ldots\}$. The determinant Φ_I of Eq. (1) is built from the occupied orbitals only,

$$|\Psi\rangle = \sum_I |\Phi_I\rangle C_I, \tag{A3}$$

$$|\Phi_I\rangle = \prod_\sigma \prod_p (\hat{a}^\dagger_{p\sigma})^{I_{p\sigma}}|0\rangle, \tag{A4}$$

where $|0\rangle$ represents the vacuum state, $I_{p\sigma} = \{0, 1\}$, and $\sum_\sigma \sum_p I_{p\sigma} = N$.

Time derivatives of orbitals are conveniently represented by the Hermitian one-electron operator $\hat{X}$ [35, 60]

$$i|\dot{\psi}_p\rangle = \hat{X}|\psi_p\rangle, \quad \hat{X} = \sum_{\mu\nu} X_\nu^\mu \hat{E}_\nu^\mu. \tag{A5a}$$

The EOMs for the TD-MCSCF method are derived based on the time-dependent variational principle, i.e., by requiring the action integral of Eq. (8) to be stationary with respect to the variation of CI coefficients and orbitals, $\partial S/\partial C_I = 0$, $\partial S/\partial \Delta_{\mu\nu} = 0$, where $\Delta_{\mu\nu}$ is an anti-Hermitian matrix generating orthonormality-conserving variations of orbitals as $\delta\psi_p = \sum_\mu \psi_\mu \Delta_{\mu p}$ [35, 41]. The resulting EOM for the CI coefficients is

$$i\dot{C}_I = \langle\Phi_I|\hat{H} - \hat{X}|\Psi\rangle, \tag{A5b}$$

and the EOMs for the orbitals Eq. (A5a) are determined by

$$\sum_{\gamma\lambda} A_{\mu\lambda}^{\nu\gamma} X_\gamma^\lambda = B_\mu^\nu, \tag{A5c}$$

where

$$A_{\mu\lambda}^{\nu\gamma} = \langle\Psi_\mu^\nu|(1-\hat{\Pi})|\Psi_\lambda^\gamma\rangle - \langle\Psi_\gamma^\lambda|(1-\hat{\Pi})|\Psi_\nu^\mu\rangle, \tag{A6}$$

$$B_\mu^\nu = \langle\Psi_\mu^\nu|(1-\hat{\Pi})\hat{H}|\Psi\rangle - \langle\Psi|\hat{H}(1-\hat{\Pi})|\Psi_\nu^\mu\rangle, \tag{A7}$$

with $|\Psi_\nu^\mu\rangle = \hat{E}_\nu^\mu|\Psi\rangle$ and $\hat{\Pi} = \sum_I |\Phi_I\rangle\langle\Phi_I|$ is the projector onto the space spanned by those Slater determinants included in Eq. (A3). Following Eqs. (A5a) and (A5b) the total time derivative of the wave function is compactly written as

$$i|\dot{\Psi}\rangle = \hat{\Pi}\hat{H}|\Psi\rangle + (1-\hat{\Pi})\hat{X}|\Psi\rangle. \tag{A8}$$

This expression shows that the time derivative of the wave function can be separated into two orthogonal contributions. The first term in Eq. (A8) gives the time evolution of the wave function in the subspace $\hat{\Pi}$ spanned by the Slater determinants $|\Phi_I\rangle$. Due to the time-dependence of the orbitals this subspace itself is time-dependent giving rise to the second term in Eq. (A8). This additional contribution directly reflects the strength of the TD-MCSCF method compared to the approach with time-independent orbitals where the evolution of the wave function is confined solely within the initial subspace. Equation (A8) shows that the component of $\hat{X}|\Psi\rangle$ that lies within $\hat{\Pi}$ cannot contribute to the evolution of the wave function. This gives rise to the distinction between *redundant* and *nonredundant* orbital pairs $\{\mu,\nu\}$. Only if $(1-\hat{\Pi})\hat{E}_\nu^\mu|\Psi\rangle \neq 0$ or $(1-\hat{\Pi})\hat{E}_\mu^\nu|\Psi\rangle \neq 0$, the matrix element X_ν^μ influences the evolution of the wave function [see Eq. (A8)] and is, therefore, called *nonredundant*. Otherwise it is called *redundant*. For redundant pairs $\{\mu,\nu\}$, as is clear from Eqs. (A6) and (A7), both $A_{\mu\lambda}^{\nu\gamma}$ and B_μ^ν vanish, thus Eq. (A5c) [or Eq. (B3c) see below] reduces to a trivial identity, and correspondingly X_μ^ν may be an arbitrary Hermitian matrix element. Therefore, Eq. (A5c) [or Eq. (B3c)] should be solved only for nonredundant pairs $\{\mu,\nu\}$.

Appendix B: Equivalent forms of EOMs

For the development of the split operator method in Sec. III B, we also present an equivalent but different form of EOMs. First we note

$$B_\mu^\nu = \sum_{\gamma\lambda} A_{\mu\lambda}^{\nu\gamma} h_\gamma^\lambda + \tilde{B}_\mu^\nu, \tag{B1}$$

where $\tilde{B}$ is given by Eq. (A7) with $\hat{H}$ replaced with $\hat{U}$. Inserting this into Eq. (A5c) and introducing an auxiliary operator

$$\hat{R} = \hat{X} - \hat{h}, \tag{B2}$$

we can rewrite Eqs. (A5) as

$$i|\dot{\psi}_p\rangle = \hat{h}|\psi_p\rangle + \hat{R}|\psi_p\rangle, \tag{B3a}$$

$$i\dot{C}_I = \langle\Phi_I|\hat{U} - \hat{R}|\Psi\rangle, \tag{B3b}$$

where $\hat{R}$ is determined by

$$\sum_{\gamma\lambda} A_{\mu\lambda}^{\nu\gamma} R_\gamma^\lambda = \tilde{B}_\mu^\nu. \tag{B3c}$$

The transformed EOMs (B3) are the generalization of those used in the variational splitting method for MCTDHF [28, 51, 52]. Yet another form of the EOMs can be derived by splitting off only the time-independent atomic Hamiltonian $\hat{h}_0$ instead of $\hat{h}$. We have implemented various choices for the EOMs and the redundant matrix elements X_ν^μ, R_ν^μ. Among them, the second form Eq. (B3), with the split-operator method described in Sec. III B, was found generally most robust. In this case, all stiff derivative operators (kinetic energy and laser-electron interaction in VG) and the singular nucleus-electron interaction are treated with the stable implicit method. The EOMs Eq. (9) for the TD-CASSCF method are obtained by applying the general TD-MCSCF EOMs (B3) to the following CASSCF ansatz for the total wave function,

$$|\Psi_{\mathrm{CAS}}\rangle = \hat{\Phi}_{\mathrm{fc}}\hat{\Phi}_{\mathrm{dc}} \sum_I |\Phi_I\rangle C_I, \tag{B4}$$

where $\hat{\Phi}_{\mathrm{fc}} \equiv \prod_i^{\mathrm{FC}} \hat{a}_{i\uparrow}^\dagger \hat{a}_{i\downarrow}^\dagger$, $\hat{\Phi}_{\mathrm{dc}} \equiv \prod_i^{\mathrm{DC}} \hat{a}_{i\uparrow}^\dagger \hat{a}_{i\downarrow}^\dagger$, and $|\Phi_I\rangle = \prod_\sigma \prod_t (\hat{a}_{t\sigma}^\dagger)^{I_{t\sigma}}|0\rangle$, with $\sum_{t\sigma} I_{t\sigma} = N_{\mathrm{a}}$. There still remains the freedom to choose the redundant part of $\hat{R}$, which is set to zero in Eqs. (9).

Appendix C: Conservation of the orbital magnetic quantum number

We require that, *at any given time t*, both the total wave function $|\Psi\rangle$ and each spatial orbital $|\psi_\mu\rangle$, are eigenfunctions of the component of the orbital angular momentum parallel to the laser polarization direction (z-axis),

$$\hat{l}_z = -i \sum_{\mu\nu} \hat{E}_\nu^\mu \int d\boldsymbol{r} \psi_\mu^*(\boldsymbol{r}) \frac{\partial}{\partial\phi} \psi_\nu(\boldsymbol{r}), \tag{C1}$$

with eigenvalues $M_{\rm tot}$ and $\{m_\mu\}$, respectively. We show that within the framework of general TD-MCSCF methods and for interactions which are rotationally symmetric about the z-axis (e.g, laser-matter interaction with linear polarization along the z-axis) $M_{\rm tot}$ as well as m_μ are constant for all times. We note that the total Hamiltonian $\hat{H}$ commutes with $\hat{l}_z$, and any two eigenstates of $\hat{l}_z$, $(|\Psi'\rangle, |\Psi''\rangle)$ with different eigenvalues M', M'' are orthogonal to each other. Thus, $\hat{l}_z$ also commutes with the CI-space projector $\hat{\Pi}$. Now we consider Eq. (A5c), which is solved for nonredundant pairs $\{\mu, \nu\}$ as

$$X_\mu^\nu = \sum_{\gamma\lambda} (A^{-1})_{\mu\lambda}^{\nu\gamma} B_\gamma^\lambda, \tag{C2}$$

where A^{-1} and B are regarded as a matrix and a vector, respectively. The element B_γ^λ is nonzero only if $m_\gamma = m_\lambda$, since otherwise the state $|\Psi_\lambda^\gamma\rangle = \hat{E}_\lambda^\gamma|\Psi\rangle$ would have an eigenvalue different from $M_{\rm tot}$,

$$\hat{l}_z|\Psi_\lambda^\gamma\rangle = (M_{\rm tot} + m_\gamma - m_\lambda)|\Psi_\lambda^\gamma\rangle. \tag{C3}$$

A similar argument applied to Eq. (A6) yields that the element $A_{\mu\lambda}^{\nu\gamma}$, and thus $(A^{-1})_{\mu\lambda}^{\nu\gamma}$, is nonzero only if $m_\mu - m_\nu = m_\lambda - m_\gamma$. Consequently, X_μ^ν [Eq. (C2)] vanishes if $m_\mu \neq m_\nu$. As a result, orbitals propagated according to Eq. (A5a) conserve $\{m_\mu\}$. Now, it follows from Eq. (A8) that $\hat{l}_z|\dot{\Psi}\rangle = M_{\rm tot}|\dot{\Psi}\rangle$, since $[\hat{l}_z, \hat{X}] = 0$. Therefore, the total projection $M_{\rm tot}$ is also conserved.

Appendix D: Ehrenfest theorem for the TD-MCSCF method

We consider the time derivative $d\langle\hat{O}\rangle/dt = d\langle\Psi|\hat{O}|\Psi\rangle/dt$ of the expectation value of an operator $\hat{O}$,

$$\frac{d}{dt}\langle\hat{O}\rangle = \langle\dot{\Psi}|\hat{O}|\Psi\rangle + \langle\Psi|\hat{O}|\dot{\Psi}\rangle + \langle\Psi|\frac{\partial\hat{O}}{\partial t}|\Psi\rangle. \tag{D1}$$

For an exact solution of the TDSE, inserting $i|\dot{\Psi}\rangle = \hat{H}|\Psi\rangle$ and its hermitian conjugate into Eq. (D1), one can derive the Ehrenfest theorem,

$$i\frac{d}{dt}\langle\hat{O}\rangle = \langle\Psi|[\hat{O}, \hat{H}]|\Psi\rangle + i\langle\Psi|\frac{\partial\hat{O}}{\partial t}|\Psi\rangle. \tag{D2}$$

For the TD-MCSCF method, inserting Eq. (A8) and its hermitian conjugate into Eq. (D1), one obtains

$$\begin{aligned} i\frac{d}{dt}\langle\hat{O}\rangle &= \langle\Psi|\hat{O}\hat{\Pi}\hat{H} - \hat{H}\hat{\Pi}\hat{O}|\Psi\rangle \\ &\quad + \langle\Psi|\hat{O}(1-\hat{\Pi})\hat{X} - \hat{X}(1-\hat{\Pi})\hat{O}|\Psi\rangle + i\langle\Psi|\frac{\partial\hat{O}}{\partial t}|\Psi\rangle \\ &= \langle\Psi|[\hat{O}, \hat{H}]|\Psi\rangle + i\langle\Psi|\frac{\partial\hat{O}}{\partial t}|\Psi\rangle \\ &\quad + \sum_{\mu\nu}\left(\sum_{\gamma\lambda} A_{\mu\lambda}^{\nu\gamma} X_\gamma^\lambda - B_\mu^\nu\right) O_{\mu\nu}, \\ &= \langle\Psi|[\hat{O}, \hat{H}]|\Psi\rangle + i\langle\Psi|\frac{\partial\hat{O}}{\partial t}|\Psi\rangle + i\Delta(\dot{O}), \end{aligned} \tag{D3}$$

where the orbital EOMs of TD-MCSCF, Eqs. (A5c)-(A7), are used for the second equality. The third line defines the quantity $\Delta(\dot{O})$, representing the difference from the Ehrenfest expression (D2),

$$\Delta(\dot{O}) = -i\sum_{\mu\nu}\left(\sum_{\gamma\lambda} A_{\mu\lambda}^{\nu\gamma} X_\gamma^\lambda - B_\mu^\nu\right) O_\nu^\mu. \tag{D4}$$

In the absence of frozen-core orbitals, Eq. (A5c) holds for all nonredundant pairs $\{\mu, \nu\}$, thus $\Delta(\dot{O}) = 0$, and Eq. (D3) reduces to Eq. (D2). This establishes the applicability of the Ehrenfest theorem to TD-MCSCF wave functions. With frozen-core orbitals $\{\psi_k\}$, however, the equality (A5c) does not hold for pairs $\{\mu, k\}$ and $\{k, \mu\}$, and thus $\Delta(\dot{O}) \neq 0$. Instead we have

$$\begin{aligned} \Delta(\dot{O}) &= i\sum_{k\mu} O_\mu^k \langle\Psi|[\hat{E}_k^\mu, \hat{H} - \hat{X}]|\Psi\rangle \\ &\quad + i\sum_{k\mu} O_k^\mu \langle\Psi|[\hat{E}_\mu^k, \hat{H} - \hat{X}]|\Psi\rangle \\ &= 2i\sum_k \langle\psi_k|\left[\hat{O}, \hat{h} + \hat{F} - \hat{X}\right]|\psi_k\rangle - 2{\rm Im}\sum_{kp} O_p^k B_k^p, \end{aligned} \tag{D5}$$

where $B_k^p = \sum_q (h_k^q + F_k^q - X_k^q) D_q^p$. For a simple physical interpretation of Δ, we consider the LG and temporarily neglect the indistinguishability of core and active electrons. In this case Eq. (D5) reduces to

$$\Delta(\dot{O}) \approx i\langle\Phi_{\rm fc}|[\hat{O}, \hat{h} + \hat{V}_{\rm a}]|\Phi_{\rm fc}\rangle, \tag{D6}$$

where $\Phi_{\rm fc}$ is the FC part of the wave function, and $\hat{V}_{\rm a}$ is the electrostatic potential of active electrons, given in real space as

$$V_{\rm a}(\boldsymbol{r}) = \int d\boldsymbol{r}' \frac{\rho_{\rm a}(\boldsymbol{r}')}{|\boldsymbol{r} - \boldsymbol{r}'|}, \tag{D7}$$

with $\rho_{\rm a}$ being the density of active electrons. Within this approximation, we obtain,

$$\Delta(\dot{z}) \approx \langle\Phi_{\rm fc}|\frac{\partial\hat{h}}{\partial p_z}|\Phi_{\rm fc}\rangle = \langle\Phi_{\rm fc}|\hat{v}|\Phi_{\rm fc}\rangle, \tag{D8}$$

$$\Delta(\dot{p}_z) \approx \langle\Phi_{\rm fc}|\frac{\partial\hat{V}_0}{\partial z} + \frac{\partial\hat{V}_{\rm ext}}{\partial z} + \frac{\partial\hat{V}_{\rm a}}{\partial z}|\Phi_{\rm fc}\rangle. \tag{D9}$$

The FC expectation value of the kinematic momentum operator $\hat{v}$ [Eq. (D8)] is time independent in general and vanishes for atomic systems, i.e., $\Delta(\dot{z}) \approx 0$. Equation (D9) can be interpreted as the binding force $f_{\rm b}$ discussed in Sec. IV B,

$$f_{\rm b} = -f_{\rm nc} - f_{\rm lc} - f_{\rm ac}. \tag{D10}$$

Appendix E: Matrix elements in the spherical-FEDVR basis

Nonzero matrix elements of one-electron operators in the spherical-FEDVR basis read

$$(\boldsymbol{h}_0)_{k'lm}^{klm} = -\frac{1}{2}\nabla_{kk'}^2 + \delta_{kk'}\left\{\frac{l(l+1)}{2r_k^2} - \frac{Z}{r_k}\right\}, \tag{E1}$$

$$(\boldsymbol{V}_{\rm ext}^{\rm LG})_{kl'm}^{klm} = r_k E(t)\alpha_{lm}, \tag{E2}$$

$$(\boldsymbol{V}_{\rm ext}^{\rm VG})_{k'l'm}^{klm} = -iA(t)\left\{\nabla_{kk'} - \delta_{kk'}\frac{(l+1)}{r_k}\right\}\alpha_{lm}, \tag{E3}$$

$$\alpha_{lm} = \sqrt{\frac{(l+1)^2-m^2}{(2l+1)(2l+3)}}, \tag{E4}$$

where $l' = l+1$ and $(\boldsymbol{V}_{\rm ext})_{klm}^{k'l'm} = (\boldsymbol{V}_{\rm ext})_{k'l'm}^{klm*}$. The matrix representations of radial derivative operators, $\nabla_{kk'} = \langle f_k|\nabla_r|f_{k'}\rangle$ and $\nabla^2_{kk'} = \langle f_k|\nabla^2_r|f_{k'}\rangle$, are sparse due to the division of the radial coordinate into finite elements, consisting of $K_{\rm FE}$ submatrices of the dimension $K_{\rm DVR}\times K_{\rm DVR}$, with adjacent submatrices overlapping at only one diagonal element corresponding to the bridge function. We treat them as banded matrices with the bandwidth $2K_{\rm DVR}+1$. See, e.g., Ref. [47] for more details.

The operator $W_q^p(r_k,\theta_j)$ (see Eq. 11) describing the electron-electron interaction is evaluated as follows. First we transform orbitals into the two-dimensional (r_k,θ_j) grid representation,

$$\varphi_p(r_k,\theta_j) = \frac{1}{\sqrt{w_k^{\rm rad}}}\sum_{l=|m_p|}^{L_{\rm max}} G_{j,lm_p}\boldsymbol{\varphi}_p^{kl}, \tag{E5}$$

where $G_{j,lm} = P_{lm}(\cos\theta_j)$, P_{lm} is an associated Legendre polynomial, and $\{\cos\theta_j\}$ and $\{w_j^{\rm ang}\}$ (appearing below) are the nodes and weights of the Gauss-Legendre quadrature, respectively, of order $L_{\rm ee}$. Note that the original three-dimensional orbital is given by $\psi_p(r,\theta,\phi) = e^{im_p\phi}\varphi_p(r,\theta)/r$. Next, the pair densities $\{\rho_q^p \equiv \varphi_p^*\varphi_q\}$ are obtained by multiplications on the grid, and transformed back into the kl basis,

$$(\boldsymbol{\rho}_q^p)_{kl} = \sum_{j=0}^{L_{\rm ee}} G^{-1}_{lM_q^p,j}\rho_q^p(r_k,\theta_j), \tag{E6}$$

where $G^{-1}_{lm,j} = w_j^{\rm ang}P^*_{lm}(\cos\theta_j)$, and $M_q^p = -m_p+m_q$. The transformed pair densities serve as the source for the radial Poisson equation [32, 45] for each partial wave lM_q^p,

$$\sum_{k'}\left\{\nabla^2_{kk'} - \delta_{kk'}\frac{l(l+1)}{r_k^2}\right\}(\boldsymbol{W}_q^p)_{k'l} = -\frac{4\pi(\boldsymbol{\rho}_q^p)_{kl}}{r_k\sqrt{w_k^{\rm rad}}}. \tag{E7}$$

We solve this equation under the boundary condition $(\boldsymbol{W}_q^p)_{K_{\rm rad}l} = \sqrt{w_{K_{\rm rad}}}/R^l$ [45], obtaining the mean field as

$$W_q^p(r_k,\theta_j) = \frac{1}{r_k\sqrt{w_k^{\rm rad}}}\sum_{l=|M_q^p|}^{L_{\rm ee}} G_{j,lM_q^p}(\boldsymbol{W}_q^p)_{kl}, \tag{E8}$$

which satisfies $W_q^p(r,\theta,\phi) = e^{iM_q^p\phi}W_q^p(r,\theta)$. Due to the sparsity of the kernel $\nabla^2_{kk'}$, the Poisson equation for each partial wave can be solved efficiently with the computational cost scaling linearly with respect to the number of radial grid points $K_{\rm rad}$.

Finally, the two-electron part $\boldsymbol{F}\boldsymbol{\varphi}_p$ of Eq. (19) is evaluated as

$$\boldsymbol{F}\varphi_p(r_k,\theta_j) = \sum_{oqsr}(D^{-1})_p^o P_{or}^{qs}W_s^r(r_k,\theta_j)\varphi_q(r_k,\theta_j) \tag{E9}$$

and transformed back into the spherical-FEDVR basis,

$$\boldsymbol{F}\boldsymbol{\varphi}_{p,kl} = \sum_{j=0}^{L_{\rm ee}} G^{-1}_{lm_p,j}\boldsymbol{F}\varphi_p(r_k,\theta_j). \tag{E10}$$

When we use FC orbitals, their contribution $\boldsymbol{F}_{\rm fc}$ to the full operator $\boldsymbol{F}$ is treated separately,

$$\begin{aligned}\boldsymbol{F}_{\rm fc}\varphi_p(r_k,\theta_j,t) &= \varphi_p(r_k,\theta_j,t)V_{\rm fc}(r_k,\theta_j,t=0)\\ &\quad - \sum_i^{\rm fc}\varphi_i(r_k,\theta_j,t)W_p^i(r_k,\theta_j,t),\end{aligned} \tag{E11}$$

where the first Coulomb term $V_{\rm fc} = 2\sum_i^{\rm fc}W_i^i$ is evaluated once in the beginning of the simulation and serves as a multiplicative operator, while the second exchange term is evaluated at each time step t, with the transformation Eq. (14) for VG simulations. The exchange term W_p^i is evaluated only within a sphere $r_k < R_i^{\rm fc}$, where $R_i^{\rm fc}$ is once determined for each FC orbital φ_i so that $|\varphi_i(R_i^{\rm fc})|$ is below a given threshold $\delta^{\rm fc}$. In this work we use $\delta^{\rm fc} = 10^{-15}$.

[1] J. Itatani, J. Levesque, D. Zeidler, H. Niikura, H. Pépin, J. C. Kieffer, P. B. Corkum, and D. M. Villeneuve, Nature **432**, 867 (2004).
[2] S. Haessler, J. Caillat, W. Boutu, C. Giovanetti-Teixeira, T. Ruchon, T. Auguste, Z. Diveki, P. Breger, A. Maquet, B. Carré, R. Taïeb, and P. Salières, Nature Phys. **6**, 200 (2010).
[3] P. Salières, A. Maquet, S. Haessler, J. Caillat, and R. Taïeb, Rep. Prog. Phys. **75**, 062401 (2012).
[4] P. Agostini and L. F. DiMauro, Rep. Prog. Phys. **67**, 813 (2004).
[5] F. Krausz and M. Ivanov, Rev. Mod. Phys. **81**, 163 (2009).
[6] L. Gallmann, C. Cirelli, and U. Keller, Annu. Rev. Phys. Chem. **63**, 447 (2013).
[7] T. Sekikawa, A. Kosuge, T. Kanai, and S. Watanabe, Nature (London) **432**, 605 (2004).
[8] Y. Nabekawa, H. Hasegawa, E. J. Takahashi, and K. Midorikawa, Phys. Rev. Lett. **94**, 043001 (2005).
[9] M. S. Pindzola and F. Robicheaux, Phys. Rev. A **57**, 318 (1998).
[10] M. S. Pindzola and F. Robicheaux, J. Phys. B **31**, L823 (1998).
[11] J. Colgan, M. S. Pindzola, and F. Robicheaux, J. Phys. B **34**, L457 (2001).
[12] J. S. Parker, L. R. Moore, K. J. Meharg, D. Dundas, and K. T. Taylor, J. Phys. B **34**, L69 (2001).

[13] S. Laulan and H. Bachau, Phys. Rev. A **68**, 013409 (2003).
[14] B. Piraux, J. Bauer, S. Laulan, and H. Bachau, Eur. Phys. J. D **26**, 7 (2003).
[15] S. Laulan and H. Bachau, Phys. Rev. A **69**, 033408 (2004).
[16] K. L. Ishikawa and K. Midorikawa, Phys. Rev. A **72**, 013407 (2005).
[17] J. Feist, S. Nagele, R. Pazourek, E. Persson, B. I. Schneider, L. A. Collins, and J. Burgdörfer, Phys. Rev. Lett. **103**, 063002 (2009).
[18] R. Pazourek, J. Feist, S. Nagele, E. Persson, B. I. Schneider, L. A. Collins, and J. Burgdörfer, Phys. Rev. A **83**, 053418 (2011).
[19] K. L. Ishikawa and K. Ueda, Phys. Rev. Lett. **108**, 033003 (2012).
[20] S. Sukiasyan, K. L. Ishikawa, and M. Ivanov, Phys. Rev. A **86**, 033423 (2012).
[21] K. L. Ishikawa and K. Ueda, Appl. Sci. **3**, 189 (2013).
[22] W. Vanroose, D. A. Horner, F. Martín, T. N. Rescigno, and C. W. McCurdy, Phys. Rev. A **74**, 052702 (2006).
[23] D. A. Horner, S. Miyabe, T. N. Rescigno, C. W. McCurdy, F. Morales, and F. Martín, Phys. Rev. Lett. **101**, 183002 (2008).
[24] T.-G. Lee, M. S. Pindzola, and F. Robicheaux, J. Phys. B **43**, 165601 (2010).
[25] J. Zanghellini, M. Kitzler, C. Fabian, T. Brabec, and A. Scrinzi, Laser Physics **13**, 1064 (2003).
[26] J. Zanghellini, M. Kitzler, T. Brabec, and A. Scrinzi, J. Phys. B **37**, 763 (2004).
[27] T. Kato and H. Kono, Chem. Phys. Lett. **392**, 533 (2004).
[28] J. Caillat, J. Zanghellini, M. Kitzler, O. Koch, W. Kreuzer, and A. Scrinzi, Phys. Rev. A **71**, 012712 (2005).
[29] M. Nest, T. Klamroth, and P. Saalfrank, J. Chem. Phys. **122**, 124102 (2005).
[30] G. Jordan, J. Caillat, C. Ede, and A. Scrinzi, J. Phys. B **39**, S341 (2006).
[31] T. Kato and H. Kono, J. Chem. Phys. **128**, 184102 (2008).
[32] D. Hochstuhl and M. Bonitz, J. Chem. Phys. **134**, 084106 (2011).
[33] D. J. Haxton, K. V. Lawler, and C. W. McCurdy, Phys. Rev. A **86**, 013406 (2012).
[34] D. J. Haxton and C. W. McCurdy, Phys. Rev. A **90**, 053426 (2014).
[35] T. Sato and K. L. Ishikawa, Phys. Rev. A **88**, 023402 (2013).
[36] K. C. Kulander, Phys. Rev. A **36**, 2726 (1987).
[37] K. L. Ishikawa and T. Sato, IEEE J. Sel. Topics Quantum Electron **21**, 8700916 (2015).
[38] T. Helgaker, P. Jørgensen, and J. Olsen, Molecular Electronic-Structure Theory (Wiley, 2002).
[39] H. Miyagi and L. B. Madsen, Phys. Rev. A **89**, 063416 (2014).
[40] D. J. Haxton and C. W. McCurdy, Phys. Rev. A **91**, 012509 (2015).
[41] T. Sato and K. L. Ishikawa, Phys. Rev. A **91**, 023417 (2015).
[42] M. Nurhuda and F. H. M. Faisal, Phys. Rev. A **60**, 3125 (1999).
[43] A. N. Grum-Grzhimailo, B. Abeln, K. Bartschat, D. Weflen, and T. Urness, Phys. Rev. A **81**, 043408 (2010).
[44] T. N. Rescigno and C. W. McCurdy, Phys. Rev. A **62**, 032706 (2000).
[45] C. W. McCurdy and M. B. N. Rescigno, J. Phys. B: At. Mol. Opt. Phys. **37**, R137 (2004).
[46] B. I. Schneider, L. A. Collins, and S. X. Hu, Phys. Rev. E **73**, 036708 (2006).
[47] B. I. Schneider, J. Feist, S. Nagele, R. Pazourek, S. X. Hu, L. A. Collins, and J. Burgdörfer, in Quantum Dynamic Imaging, edited by A. D. Bandrauk and M. Ivanov (Springer, New York, 2011) pp. 149–208.
[48] J. Frenkel, Wave Mechanics-Advanced General Theory (Oxford at the Clarendon Press, 1934).
[49] P.-O. Löwdin and P. K. Mukherjee, Chem. Phys. Lett. **14**, 1 (1972).
[50] R. Moccia, Int. J. Quantum Chem. **7**, 779 (1973).
[51] C. Lubich, Appl. Numer. Math. **48**, 355 (2004).
[52] O. Koch and C. Lubich, IMA Journal of Numerical Analysis **31**, 379 (2010).
[53] M. V. Ammosov, N. B. Delone, and V. P. Kraĭnov, Sov. Phys. JETP **64**, 1191 (1986).
[54] A. M. Perelomov, V. S. Popov, and M. V. Terentev, Sov. Phys. JETP **23**, 924 (1966).
[55] A. Gordon, F. X. Kärtner, N. Rohringer, and R. Santra, Phys. Rev. Lett. **96**, 223902 (2006).
[56] M. Lewenstein, P. Balcou, M. Y. Ivanov, A. L'Huillier, and P. B. Corkum, Phys. Rev. A **49**, 2117 (1994).
[57] K. C. Kulander, K. J. Schafer, and J. L. Krause, in Atoms in Intense Laser Fields, edited by M. Gavrila (Academic Press, New York, 1992) pp. 247–300.
[58] R. Sawada, T. Sato, and K. L. Ishikawa, Phys. Rev. A **93**, 023434 (2016).
[59] F. Lackner, I. Březinová, T. Sato, K. L. Ishikawa, and J. Burgdörfer, Phys. Rev. A **91**, 023412 (2015).
[60] R. P. Miranda, A. J. Fisher, L. Stella, and A. P. Horsfield, J. Chem. Phys. **134**, 244101 (2011).